ORIGINAL ARTICLE

Optimized protocols for cardiac magnetic resonance imaging in patients with thoracic metallic implants

Laura J. Olivieri[1,2] · Russell R. Cross[1] · Kendall E. O'Brien[1] ·
Kanishka Ratnayaka[1,2] · Michael S. Hansen[2]

Abstract

Background Cardiac magnetic resonance (MR) imaging is a valuable tool in congenital heart disease; however patients frequently have metal devices in the chest from the treatment of their disease that complicate imaging. Methods are needed to improve imaging around metal implants near the heart. Basic sequence parameter manipulations have the potential to minimize artifact while limiting effects on image resolution and quality.

Objective Our objective was to design cine and static cardiac imaging sequences to minimize metal artifact while maintaining image quality.

Materials and methods Using systematic variation of standard imaging parameters on a fluid-filled phantom containing commonly used metal cardiac devices, we developed optimized sequences for steady-state free precession (SSFP), gradient recalled echo (GRE) cine imaging, and turbo spin-echo (TSE) black-blood imaging. We imaged 17 consecutive patients undergoing routine cardiac MR with 25 metal implants of various origins using both standard and optimized imaging protocols for a given slice position. We rated images for quality and metal artifact size by measuring metal artifact in two orthogonal planes within the image.

Results All metal artifacts were reduced with optimized imaging. The average metal artifact reduction for the optimized SSFP cine was $1.5 +/- 1.8$ mm, and for the optimized GRE cine the reduction was $4.6 +/- 4.5$ mm ($P < 0.05$). Quality ratings favored the optimized GRE cine. Similarly, the average metal artifact reduction for the optimized TSE images was $1.6 +/- 1.7$ mm ($P < 0.05$), and quality ratings favored the optimized TSE imaging.

Conclusion Imaging sequences tailored to minimize metal artifact are easily created by modifying basic sequence parameters, and images are superior to standard imaging sequences in both quality and artifact size. Specifically, for optimized cine imaging a GRE sequence should be used with settings that favor short echo time, i.e. flow compensation off, weak asymmetrical echo and a relatively high receiver bandwidth. For static black-blood imaging, a TSE sequence should be used with fat saturation turned off and high receiver bandwidth.

Keywords Artifact · Children · Congenital heart disease · Heart · Magnetic resonance imaging · Metal

Introduction

Clinical relevance

People with congenital heart disease frequently have metal devices placed in the chest surgically or percutaneously for treatment of a variety of structural and electrical cardiac diseases [1]. The majority of these devices are not contraindications to cardiac MR imaging [2] but present significant challenges to imaging because the presence of metal in the static magnetic field dephases the local magnetization, causing signal loss in the image. The need for improved MR imaging techniques in structures near metal is a recognized problem in many populations, from imaging renal arteries to imaging coronary arteries in adults with coronary disease [3–8].

✉ Laura J. Olivieri
lolivier@childrensnational.org

1   Division of Cardiology, Children's National Health System,
    W3-200, 111 Michigan Ave. NW,
    Washington, DC 20010, USA

2   National Heart, Lung and Blood Institute,
    National Institutes of Health,
    Bethesda, MD, USA

Although a large amount of work has been dedicated to ensuring MR safety of various metal cardiac devices [9–12], less work has been dedicated to develop techniques to improve images around these metal devices.

The scope of the problem is compounded by the fact that serial MR imaging is proving useful in many conditions [13–15]. Preliminary work has acknowledged this issue in the imaging of patients with congenital heart disease [16, 17]. For example, sternal wires frequently obscure the border of an anterior aorta or neo-aorta, portions of a Fontan are obscured by septal occluders placed in the fenestration, and branch pulmonary arteries are obscured by bare metal stents. This limits the availability of critical information for deciding when an intervention is needed and for planning a surgical or percutaneous intervention. Because of the widespread use of metal devices, improved survival of this patient population and an accumulating body of evidence demonstrating the value of serial cardiac MR imaging, simple techniques to minimize metal artifact are needed to image this population.

Approach to imaging

When imaging structural heart disease, two of the sequences commonly used are steady-state free precession (SSFP) cine imaging and turbo spin-echo (TSE) black-blood imaging. Both of these sequences are compromised when imaging near metal, but the standard protocols can be modified to minimize the metal artifacts, albeit at the expense of signal-to-noise ratio (SNR) and possibly spatial resolution.

The metal artifact susceptibility of the SSFP sequence is largely determined by the repetition time (TR). At longer repetition times, dark band artifacts may dominate the images, even relatively far from the metal itself. To decrease the repetition time, asymmetrical or partial Fourier readouts [16] can be used. In fact many clinical SSFP protocols use asymmetrical readouts, mostly to shorten the image acquisition time. However, in the presence of large magnetic field inhomogeneities, as seen around metal implants, the use of asymmetrical echo could lead to reduced image quality and artifacts, and it could in fact be preferable to image with less aggressive asymmetrical echo settings in patients with metal implants. The pursuant increase in TR can be mitigated through an increase in sampling bandwidth, albeit at the expense of a reduction in SNR. The appropriate choice of asymmetrical echo and bandwidth may be different in the presence of metal. Finally, the SSFP readout can be changed to a spoiled gradient echo (GRE) sequence, which eliminates the TR dependency, but the GRE sequence has lower inherent SNR and also shows metal artifacts. These artifacts can be reduced by reducing the echo time (TE). Partial Fourier readout and bandwidth increases can reduce the TE at the expense of resolution and SNR.

The black-blood TSE sequence typically uses a fat suppression pulse [5], which is a frequency-selective pulse that relies on a fairly homogeneous field. In the presence of metal, the field inhomogeneities cause the fat suppression pulse to suppress water signal, which is off-resonance. For patients with metal implants, this paper explores the use of TSE sequences without fat suppression. The TSE sequence also benefits from a shorter TE when imaging near metal, in terms of both artifact size and image distortion. A shorter TE can be achieved by increasing the bandwidth, which reduces SNR.

The objective of this work was two-fold: first we aimed to develop optimized static and cine cardiac imaging protocols through systematic variation of sequence parameters to assess their effect on artifact size and image quality. Second, we aimed to demonstrate the clinical value of these optimized protocols through their use in patients with metal devices, as compared to standard cardiac imaging protocols.

Materials and methods

In vitro imaging and sequence selection

The goal of the in vitro imaging was to identify an optimal sequence to minimize metal artifact without significant compromise of image resolution or signal-to-noise ratio (SNR). Turbo spin-echo (TSE) black-blood imaging, spoiled gradient echo (GRE) cine and steady-state free precession (SSFP) cine imaging were performed on an Aera 1.5-T system (Siemens Healthcare, Erlangen, Germany) using a water-filled phantom containing four common metal cardiac devices (Fig. 1). The devices included a Palmaz Genesis stainless steel bare metal stent (Cordis, Bridgewater, NJ), an Amplatzer atrial septal occluder and an Amplatzer vascular plug (St. Jude Medical, St. Paul, MN), and stainless steel coils (Cook Medical, Bloomington, IN). Table 1 lists the sequence parameters that were varied for each of the three types of imaging. The authors judged the in vitro experiments by artifact size, reasonableness of breath-hold time, and relative image quality. Because the in vitro experiments were repetitive identical images, it was very easy to judge even small variations in artifact size by viewing them sequentially in a standard viewer and watching the artifact grow and shrink.

For SSFP imaging, the receiver bandwidth was varied at 400–1,500 Hz/pixel for strong, weak and no asymmetrical echo, which corresponded to relative echo positions of 32%, 36% and 50%, respectively. All other parameters, including flip angle, field of view (FOV) and parallel imaging acceleration factors, were held constant. The echo spacing and relative SNR were charted, and images were evaluated for quality. Baseline SNR of 1 was at a receiver bandwidth of 400 Hz/pixel.

Fig. 1 Photograph (*left*) and SSFP MR image (*right*) depict the location of the four metal devices used for in vitro imaging. The Palmaz genesis bare metal stent (Cordis, Bridgewater, NJ) is in the upper left corner, the stainless steel coil (Cook Medical, Bloomington, IN) is in the upper right corner, the Amplatzer vascular plug (St. Jude Medical, St. Paul, MN) (*vasc plug*) is in the lower left corner and the Amplatzer atrial septal occluder (St. Jude Medical, St. Paul, MN) (*ASO*) is in the lower right corner
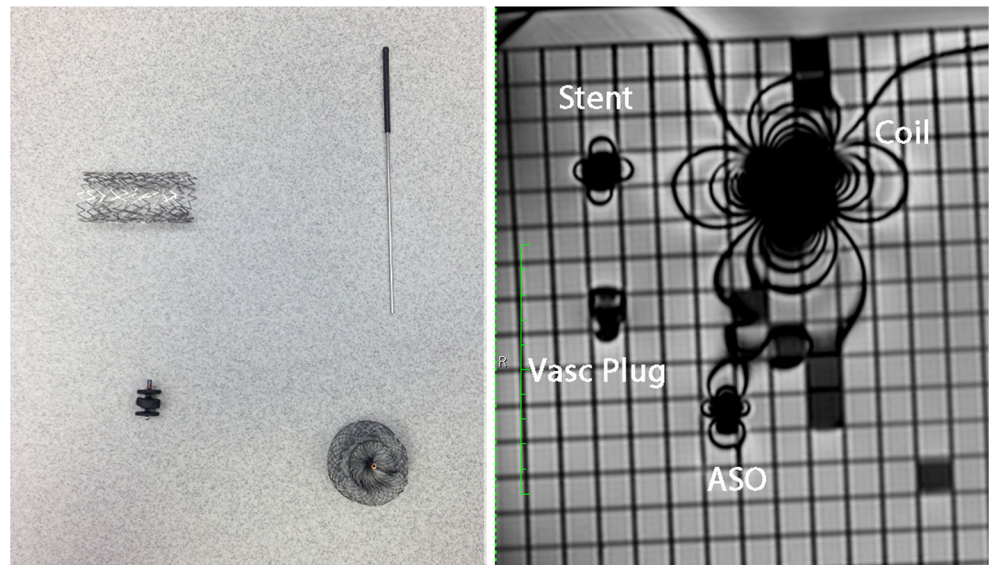
For GRE imaging, a nearly identical experiment was run, including variation of asymmetrical echo and receiver bandwidth. For GRE, strong, weak and no asymmetrical echo imaging options were completed, corresponding to relative echo positions of 35%, 40% and 50%. The TE and relative SNR were recorded, and the other imaging parameters were held constant. Flow compensation was turned off, which further decreased the echo time, and long-term averaging was increased to 3, which improved image SNR; however this tripled the breath-hold time, thus was turned off.

Finally, for TSE imaging receiver bandwidth was varied at 250–781 Hz/pixel with a fat-saturation pulse on and with a fat-saturation pulse off.

Table 1 Sequence parameters that were varied for each of the three types of imaging, including steady-state free precession (SSFP), gradient recalled echo (GRE) and turbo spin echo (TSE)

Sequence parameter	SSFP cine	GRE cine	TSE
Strong asymmetrical echo	x	x	
Weak asymmetrical echo	x	x	
Asymmetrical echo off	x	x	
*BW ~250 MHz			X
*BW ~500 MHz	x	x	x
*BW ~750 MHz			x
*BW ~1,000 MHz	x	x	x
*BW ~1,500 MHz	x	x	
Flow compensation off		x	
Flow compensation on		x	
Fat saturation off		x	
Fat saturation on		x	
Long-term averaging off			
Long-term averaging on		x	

*BW receiver bandwidths are approximate values

In vivo imaging

This work was approved by the institutional review board, and all patients gave their written informed consent to be included.

We included 17 consecutive children and adults undergoing clinically indicated, routine cardiac MR with 25 metal implants of various origins. Standard sequences for black-blood imaging and SSFP cine imaging were performed as well as the optimized sequence for SSFP cine, GRE cine and black-blood imaging, chosen from the in vitro imaging sequences. All imaging was performed at one identical slice position with identical FOV where the metal artifact was most present. TSE imaging was acquired at end-diastole. All imaging used a breath-held acquisition.

Images were then reviewed by an expert reviewer (L.O., 4 years of experience post-fellowship) blinded to the imaging protocol. The reviewer assigned a qualitative score of 1–5 (1=excellent, 5=non-diagnostic) based on features of the images including (1) blood-pool–tissue contrast, (2) metal artifact severity and (3) diagnostic quality. Additionally, a "best overall" cine image and black-blood image were selected for each slice position. Finally, the dimension of the metal artifacts was measured on all images in an identical manner, in two orthogonal planes along the long and short axes of the metal device. The measurement was made from the edges of the metal artifact, and care was taken to make the measurement location identical among images.

A score of 1 indicated the worst quality and a score of 5 indicated the best. Specifically, a score of 5 (excellent) was given if an image had no noteworthy artifacts, good contrast between blood and myocardium and sharp boundaries. A score of 4 (good) was given for images with some insignificant artifacts but good enough quality

to determine endocardial border or vessel size. A score of 3 (fair) was given to images with borderline image quality, which could still be used to evaluate global function and give a single linear measurement from a vessel on black-blood imaging. A score of 2 (poor) meant insufficient image quality to evaluate endocardial border or vessel lumen and the score of 1 (non-diagnostic) was given to images where it was impossible to evaluate endocardial border or vessel lumen on black-blood imaging. This scoring system was based on previous work with similar image comparison [18]. From this scoring system, a best image was selected from each of the three cine techniques as well as from both of the black-blood techniques.

The artifact sizes and size differences were compared with mean and standard deviation, and compared with 2-tailed *t*-tests. Additionally, absolute artifact reduction between imaging methods was tallied, and a best quality imaging method was selected for each type of imaging, cine and static black blood.

Results

In vitro imaging

Figure 2 depicts the relationship between repetition time (TR) and receiver bandwidth as well as between signal-to-noise ratio (SNR) and receiver bandwidth for SSFP imaging experiments. Figure 3 shows the in vitro imaging with the columns displaying no, weak and strong asymmetrical echo from left to right, and the rows demonstrating receiver bandwidth at 400–1,488 Hz/pixel. With increasing bandwidth, the metal artifacts reduce in size. There is also a slight tendency toward blurring with strong asymmetrical echo on, compared to off, but the in vitro experiments did not yield conclusive evidence as to which asymmetrical echo setting is preferable. An optimized SSFP sequence with receiver bandwidth of 1,488 Hz/pixel and weak asymmetrical echo was chosen for comparison with the standard SSFP sequence (strong asymmetrical echo and lower bandwidth). The two sequences had approximately the same TR (2.7 ms).

Figure 4 displays the relationship between echo time (TE) and receiver bandwidth and between SNR and receiver bandwidth for GRE imaging experiments. Figure 5 shows the in vitro imaging with the columns displaying no, weak and strong asymmetrical echo from left to right, and the rows demonstrate receiver bandwidth at 400–1,015 Hz/pixel. The optimized sequence for GRE imaging is weak asymmetrical echo, flow compensation off, bandwidth 1,015 Hz/pixel.

Finally, Fig. 6 shows the TSE imaging experiment data: the left column shows imaging with fat saturation on, the right column shows imaging with fat saturation off, and the
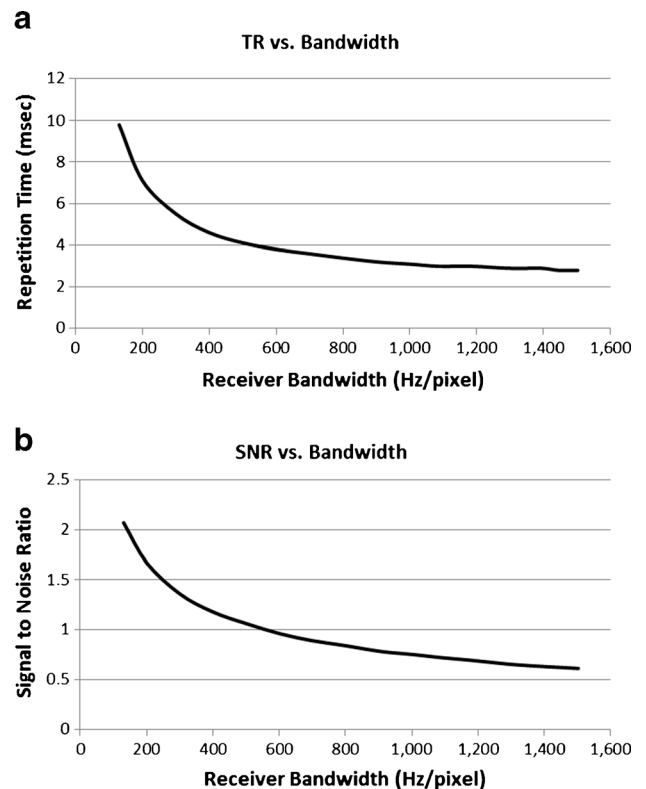
a

TR vs. Bandwidth

b

SNR vs. Bandwidth

Fig. 2 Steady-state free precession (SSFP) in vitro imaging. Graphs depict the relationship between (**a**) receiver bandwidth and repetition time (TR) and (**b**) receiver bandwidth and signal-to-noise ratio (SNR) for steady-state free precession (SSFP) imaging. As receiver bandwidth increases, the repetition time decreases, as does the SNR

bandwidth increases down the rows. The optimized sequence for TSE used a bandwidth of 781 Hz/pixel, fat suppression off.

In vivo imaging

The 17 patients ranged in age 4–43 years, with a mean age of 14.9 years and mean body surface area (BSA) 1.36 m^2. Table 2 summarizes the characteristics of the cohort, including age, BSA and the location and type of metal device imaged. Twenty-four metal devices were encountered in this population, including bare metal stents, atrial and ventricular septal occluders, vascular plugs, coils and sternal wires. Table 3 summarizes the metal artifact size and size differences among sequences. Figures 7, 8 and 9 offer in vivo imaging examples of the five techniques. At a heart rate of 80 bpm, the breath-hold times were 9.6 s for the SSFP, optimized SSFP, TSE and optimized TSE. The breath-hold time was 12 s for the optimized GRE.

Cine imaging

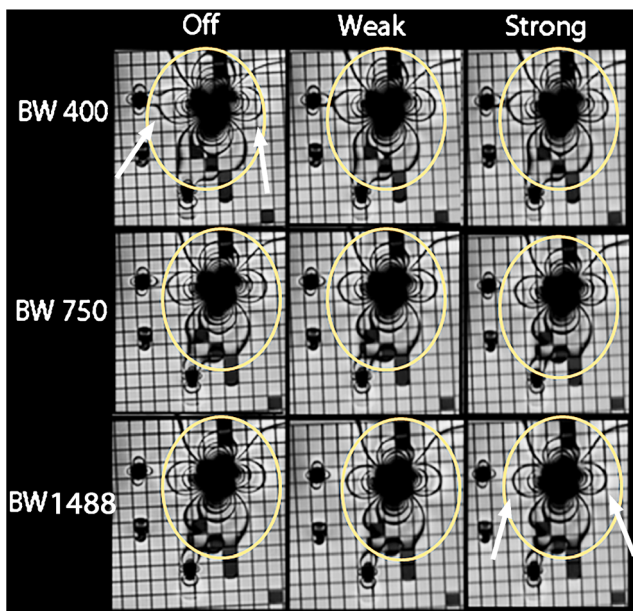The average metal artifact size was 24+/−9.6 mm, 22+/−9 mm, and 19.4+/−8.1 mm for the SSFP, optimized SSFP

Fig. 3 In vitro imaging of four metal cardiac devices using steady-state free precession (SSFP) imaging while varying the receiver bandwidth (*rows*) and asymmetrical echo strength (*columns*). Ovals represent the size of the artifact in the top left corner, and arrows indicate the changes in artifact size between the first and last images. As bandwidth increases, the image artifacts decrease and image quality decreases. As asymmetrical echo strength increases, the image artifact decreases and image quality decreases. There are significant differences between artifact sizes between the upper left and bottom right panels with similar image quality (*arrows*). For example, artifact from the bare metal stent and the coil are overlapping in the upper left image and are smaller and separate in the bottom right image

and optimized GRE cines, respectively ($P < 0.05$ for all groups). The average metal artifact reduction between the standard SSFP cine and the optimized SSFP cine was 1.5+/−1.8 mm, and the average artifact reduction between the optimized SSFP cine and the optimized GRE cine was 4.6+/−4.5 mm. Based on quality scoring, a best cine and a best black-blood image were selected among the images for each slice location. The best cine quality distribution was: SSFP 4% ($n=1$), optimized SSFP 12% ($n=3$) and optimized GRE 84% ($n=19$) (Table 3).

Static black-blood imaging

The average metal artifact size was 15.4+/−5.4 mm for standard TSE and 13.6+/−1.6 mm for the optimized TSE sequence ($P < 0.05$). The average metal artifact reduction between the standard TSE black-blood and the optimized black-blood sequences was 1.6+/−1.7 mm. Again, based on quality scoring, a best cine and a best black-blood image were selected among the images for each slice location (Table 3). The best black-blood quality distribution was standard TSE 25% ($n=5$) and optimized TSE 75% ($n=16$). There were no instances of missed diagnostic information between imaging with and without fat-saturation pulse for the TSE imaging.
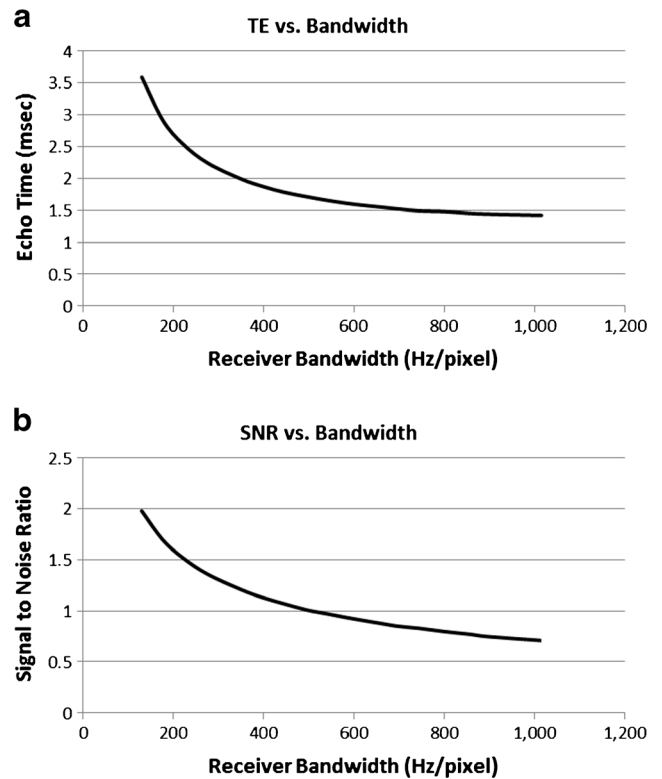

Fig. 4 Gradient recalled echo (GRE) in vitro imaging. Graphs depict the relationship between (**a**) receiver bandwidth and echo time (TE) and (**b**) receiver bandwidth and signal-to-noise ratio (SNR) for GRE imaging. As receiver bandwidth increases, the echo time decreases, as does the SNR
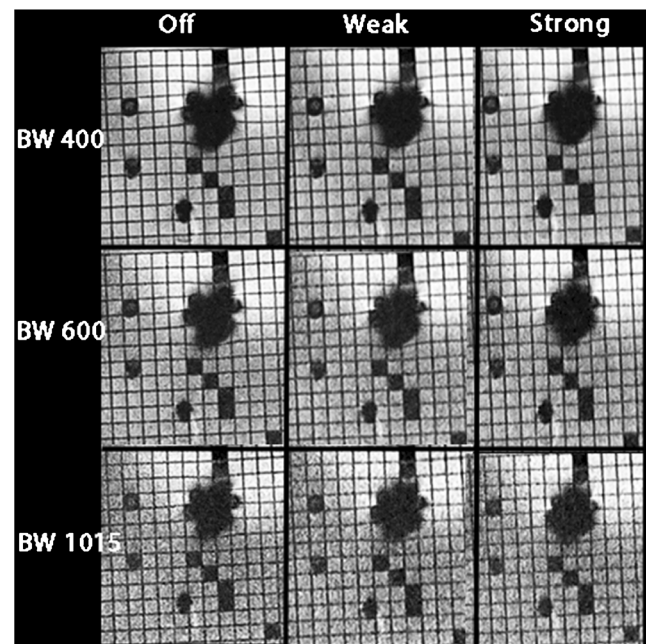

Fig. 5 In vitro imaging of four metal cardiac devices using gradient recalled echo (GRE) imaging while varying the receiver bandwidth (*rows*) and asymmetrical echo strength (*columns*). As bandwidth increases, the image artifacts decrease and image quality decreases. As asymmetrical echo strength increases, the image artifact decreases and image quality decreases. There are significant differences in artifact size between the upper left and bottom right panels, with significant compromise in image quality
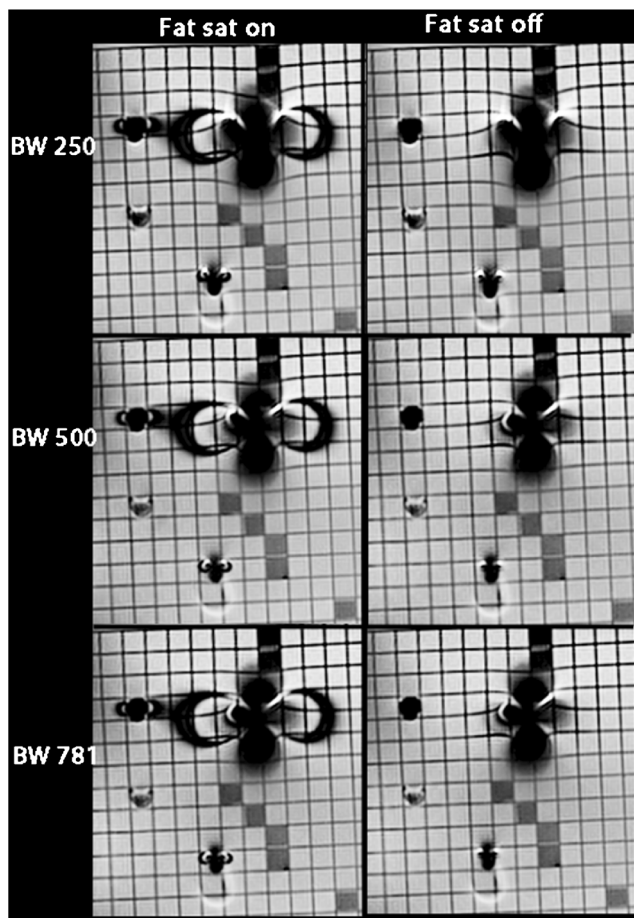
Fig. 6 In vitro imaging of four metal cardiac devices using turbo spin echo (TSE) imaging while varying the receiver bandwidth (*rows*) and turning the fat-saturation pulse on and off (left and right columns, respectively). As bandwidth increases, the image artifacts decrease and image quality decreases. When the fat-saturation pulse is turned off, the artifact significantly decreases in the phase encoding direction

Table 2 Age (years), body surface area (BSA, m^2), type of metal artifact and location of the metal implant for each device in subject in the study group

Subject	Age	BSA	Artifact	Location
1	16.4	1.8	Pulmonary valve	RVOT
2	28.0	1.7	Proximal coarct stent	Aortic isthmus
2			Distal coarct stent	Descending aorta
3	14.8	1.5	PDA coil	PDA
4	7.6	1.0	Sternal wire	Chest wall
5	8.0	1.1	Sternal wire	Chest wall
			Bare metal stent	RPA
6	4.4	0.6	Sternal wire	Chest wall
			Fenestration device	Fontan
7	12.1	1.1	Fenestration device	Fontan
8	24.4	2.0	Sternal wire	Chest wall
9	2.7	0.5	Sternal wire 1	Chest wall
			Sternal wire 2	Chest wall
			Sternal wire 3	Chest wall
10	23.8	1.8	Pulmonary valve	RVOT
11	10.7	1.2	Sternal wire	Chest wall
12	13.2	1.4	Bare metal stent	LPA
13	11.4	1.2	Sternal wire	Chest wall
14	4.2	0.6	Sternal wire	Chest wall
			Bare metal stent	RPA
15	43.3	2.0	Sternal wire	Chest wall
16	8.0	1.6	Sternal wire	Chest wall
			Bare metal stent	MPA
17	21.4	2.1	Sternal wire	Chest wall

LPA left pulmonary artery, *MPA* main pulmonary artery, *PDA* patent ductus arteriosus, *RPA* right pulmonary artery, *RVOT* right ventricular outflow tract

Discussion

Imaging around metal devices in the chest is an ever-growing issue for those who routinely care for patients with congenital heart disease; evidence supporting the value of cardiac MR, and in particular serial cardiac MR, grows every year. Therefore, improvement of cardiac imaging in the setting of multiple implants in the chest is of paramount importance. Each year, studies and guidelines are published demonstrating the ability to make difficult clinical decisions based on MR-derived measurements in children and adults with congenital heart disease. Once metal devices are implanted, they are rarely resected from the chest, thus the issue of improving MR imaging around metal artifacts is expected to become increasingly important, particularly with the growing capability of percutaneous interventions, which typically involve placement of a metal device to treat a defect that would otherwise be approached by an open-heart surgery without necessarily involving metal implants in the chest.

In this study, in vitro imaging experiments were conducted in order to understand the imaging tradeoffs between minimizing artifact and sacrificing image quality while testing the boundaries of sequence parameter variation. For SSFP and GRE imaging, the traditional trade-offs made between SNR and image quality may not be appropriate when imaging near metal implants. Specifically, a lower SNR is acceptable (as demonstrated in this paper), if metal artifacts are reduced. By making maneuvers to decrease the TR (SSFP) and TE (GRE), such as increasing the bandwidth, decreasing the amount of data filling k space and adjusting flow compensation, the reduction in metal artifact improves the image more than the decreases in resolution and SNR compromise the image. In the in vivo imaging, the optimized SSFP sequence offered only marginal differences in image quality that are likely clinically insignificant, and the SSFP and optimized SSFP repetition times were very similar. The optimized GRE cine offered significant artifact reduction. In TSE imaging, receiver bandwidth plays a role in the size of the metal

Table 3 Metal artifact size and reduction in size among sequences

Imaging method	Average artifact size (mm)*	Standard deviation (mm)	Average artifact reduction (mm)	% "best" image quality	Average Quality Rating
Standard SSFP cine	24	9.6		4%	2.2
Optimized SSFP cine	22	9	1.5	12%	2.4
Optimized GRE cine	19.4	8.1	4.6	84%	2.7
Standard TSE black blood	15.4	5.4		25%	2.8
Optimized TSE black blood	13.6	1.6	1.6	75%	3.1

GRE gradient recalled echo, SSFP steady-state free precession, TSE turbo spin echo

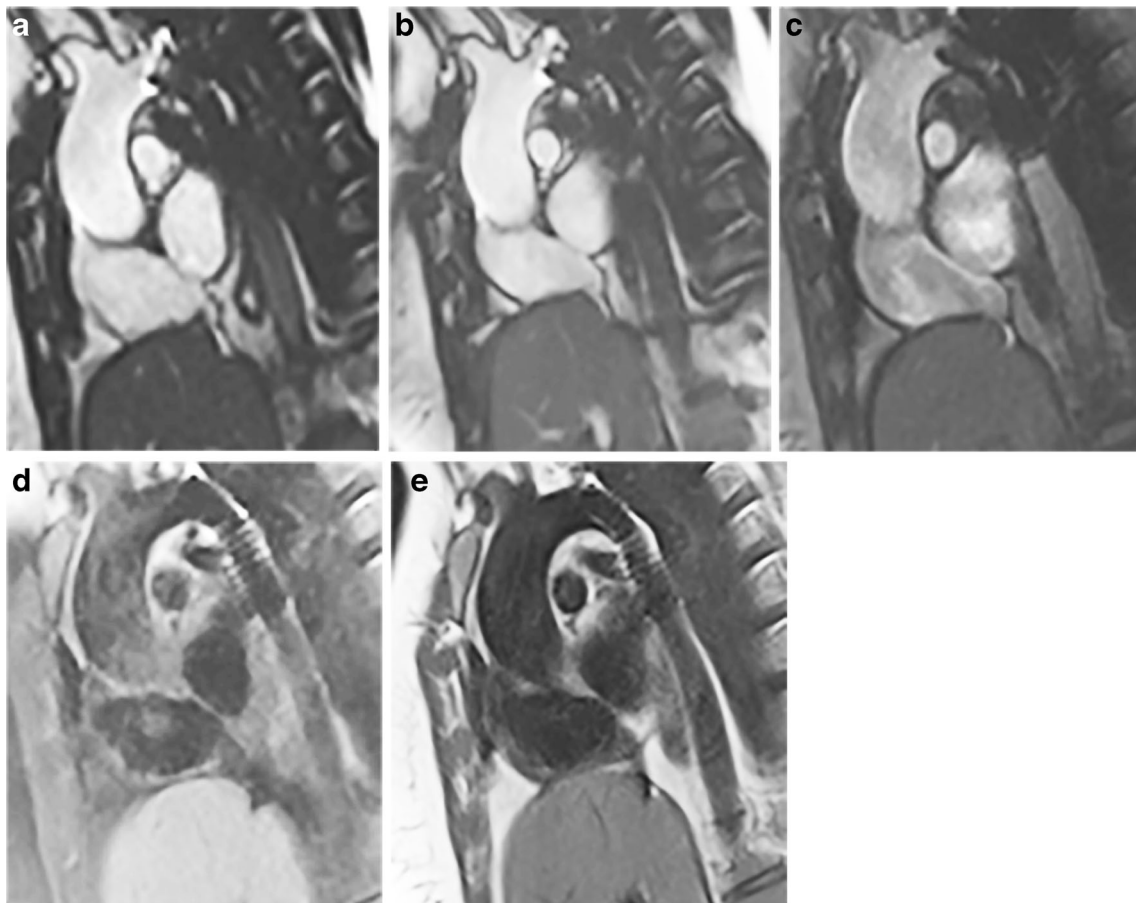*Average artifact size is the average of two orthogonal measurements of the artifact in millimeters

Fig. 7 Standard vs. optimized imaging sequences in a 28-year-old woman with two platinum stents in the aortic isthmus and proximal descending aorta. Imaging is in the parasagittal plane. **a** Standard SSFP cine (TR/TE 2.7/1.08 ms, acceleration factor 2, voxel size 0.8×0.8×6-mm reconstructed, breath-hold time 9.6 s). **b** Optimized SSFP cine (TR/TE 2.7/1.14 ms, acceleration factor 2, voxel size 0.8×0.8×6-mm reconstructed, breath-hold time 9.6 s). **c** Optimized GRE cine (TR/TE 3.82/1.69 ms, acceleration factor 2, voxel size 0.8×0.8×6-mm reconstructed, breath-hold time 12 s). **d** Standard TSE (TR/TE 740/31 ms, voxel size 1.4×1.4×4 mm, breath-hold time 9.6 s). **e** Optimized TSE (TR/TE 656/29 ms, voxel size 1.4×1.4×4 mm, breath-hold time 9.6 s). In (**a**) and (**b**), as the SSFP bandwidth increases the artifact size decreases and image quality improves. In (**c**), the dephasing artifact decreases significantly with GRE imaging with a receiver bandwidth of 1,488 Hz/pixel, flow compensation off and weak asymmetrical echo. In (**d**) and (**e**) improvement in artifact size is seen with fat saturation off and bandwidth of 781 Hz/pixel. GRE gradient recalled echo, SSFP steady-state free precession, TE echo time, TR repetition time, TSE turbo spin echo
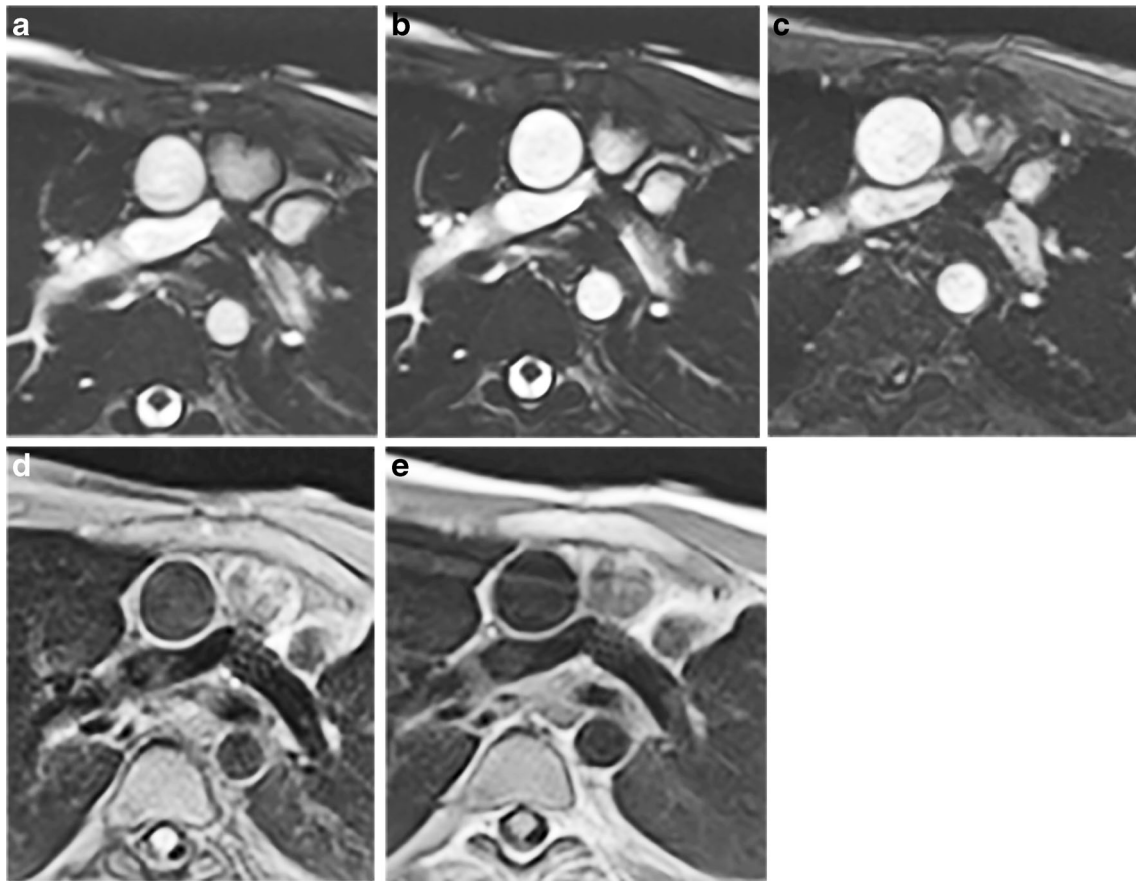
Fig. 8 Standard vs. sequences optimized for artifact reduction in a 12-year-old boy with a bare metal stent in the proximal left pulmonary artery. Imaging is in the axial plane. **a** Standard SSFP cine (TR/TE 2.7/1.1 ms, matrix 176×176, FOV 264×264 mm, acceleration factor 2, voxel size 0.8×0.8×6 mm, breath-hold time 12.7 s). **b** Optimized SSFP cine (TR/TE 2.7/1.1 ms, matrix 176×176, FOV 264×264 mm, acceleration factor 2, voxel size 0.8×0.8×6 mm, breath-hold time 12.6 s. **c** Optimized GRE cine (TR/TE 3.82/1.69 ms, matrix 176×176, FOV 264×264 mm, voxel size 0.8×0.8×6, acceleration factor 2, breath-hold 16.14 s). **d** Standard TSE (TR/TE 1,141/31 ms, matrix 192×192, FOV 240×240 mm, voxel size 1.4×1.4×4 mm, breath-hold 12.6 s). **e** Optimized TSE (TR/TE 1,131/29 ms, matrix 192×192, FOV 240×240 mm, voxel size 1.4×1.4×4 mm, breath-hold time 12.5 s). In (**c**), the dephasing artifact decreases significantly with GRE imaging with a receiver bandwidth of 1,488 Hz/pixel, flow compensation off and weak asymmetrical echo. In (**d**) and (**e**), improvement in artifact size is seen when when fat saturation is off and bandwidth is increased to 781 Hz/pixel. *FOV* field of view, *GRE* gradient recalled echo, *SSFP* steady-state free precession, *TE* echo time, *TR* repetition time, *TSE* turbo spin echo

artifact and should be chosen to provide adequate SNR. The fat-saturation pulse, which is commonly used in conjunction with TSE imaging, can cause major artifacts. Fat-saturation pulses are typically frequency-selective pulses that rely on the frequency difference between water and fat to saturate the fat signal. In the presence of metal, some of the water signal may in fact be at the fat resonance frequency and become saturated. As demonstrated in this paper, the frequency selective fat saturation should be switched off to avoid such artifacts.

In addition to artifacts, metal can cause distortion of the magnetic field and the resultant image, which could affect image interpretation and image measurements. The techniques described above also decrease field distortions in addition to decreasing metal artifact, through the same mechanisms that have been described. In this work, we did not explicitly quantify the value of this reduction in geometric distortions.

This preliminary work acknowledges the issue and demonstrates feasibility of simple product sequence modifications to minimize the impact of metal artifact. Additionally, these modifications did not seriously deteriorate image quality or require unusually long breath-holds. There are limitations to this study; we chose to focus on using out-of-the-box sequences with simple modifications instead of developing new sequences altogether, which may limit the potential for image improvement. There are factors that affect imaging quality in in vivo imaging that cannot be accounted for with in vitro imaging, such as patient body habitus, heart rate, and the effect of dephased, flowing blood in any particular image. Our work is the first in vivo testing of sequences specifically designed to diminish metal artifact by approaching basic sequence parameters. Future work in this area is needed for improved 3-D imaging,
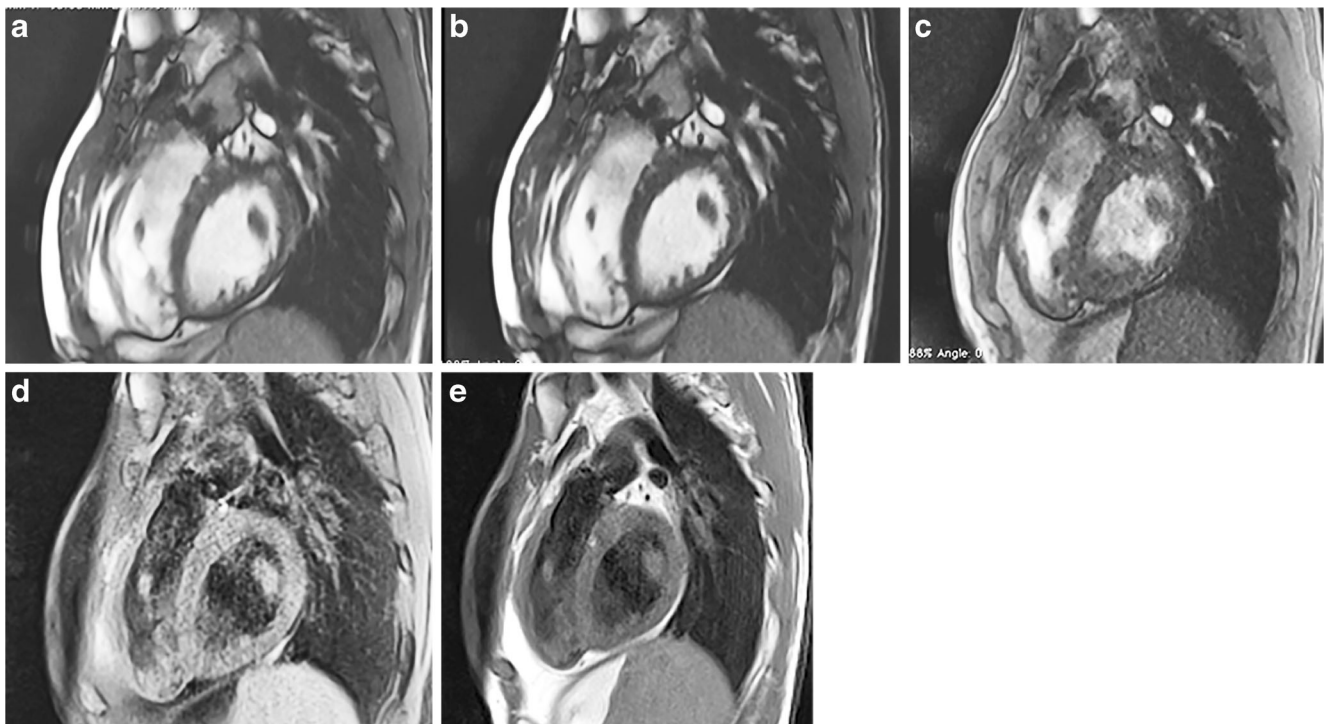
Fig. 9 Standard vs. sequences optimized to reduce metal artifact in a 23-year-old woman who had undergone repair of tetralogy of Fallot with subsequent pulmonary valve replacement. Imaging is in the sagittal plane. **a** Standard SSFP cine (TR/TE 2.7/1.1 ms, matrix 224×168, FOV 336×408 mm, acceleration factor 2, voxel size 0.8×0.8×8 mm, breath-hold time 7.6 s. **b** Optimized SSFP cine (TR/TE 2.7/1.2 ms, matrix 224×168, FOV 336×408 mm, acceleration factor 2, voxel size 0.8×0.8×8 mm, breath-hold time 7.8 s. **c** Optimized GRE cine (TR/TE 3.81/1.7 ms, matrix 224×168, FOV 336×408 mm, acceleration factor 2, voxel size 0.8×0.8×8 mm, breath-hold time 11.4 s. **d** Standard TSE (TR/TE 847/31 ms, matrix 192×256, FOV 251×335 mm, voxel 1.3×1.3×4 mm, breath-hold time 9.2 s. **e** Optimized TSE (TR/TE 830/29 ms, matrix 192×256, FOV 251×335 mm, voxel size 1.3×1.3×4 mm, breath-hold time 9.3 s). In (**c**), the dephasing artifact decreases significantly with GRE imaging with a receiver bandwidth of 1,488 Hz/pixel, flow compensation off and weak asymmetrical echo. In (**d**) and (**e**), improvement in artifact size is seen when fat saturation is off and bandwidth increased to 781 Hz/pixel. *FOV* field of view, *GRE* gradient recalled echo, *SSFP* steady-state free precession, *TE* echo time, *TR* repetition time, *TSE* turbo spin echo

artifact reduction in flow, and finally improved 4-D flow imaging.

Conclusion

Artifacts were reduced in all cases proceeding from standard to optimized static and cine imaging, without significant changes in image quality. Imaging sequences specially tailored to minimize metal artifact are superior to standard imaging sequences in both quality and size of the metal artifact. Specifically, for optimized cine imaging a GRE sequence should be used with flow compensation off, weak asymmetrical echo and a relatively high receiver bandwidth on the order of 1,000 Hz/pixel. These settings minimize echo time at the expense of some loss in signal-to-noise ratio. The loss in signal-to-noise ratio can be compensated for with averaging. For static black-blood imaging, a TSE sequence should be used with fat-saturation pulse turned off and a relatively high bandwidth. The fat-saturation pulses tend to fail near large magnetic field inhomogeneities and should not be used when imaging patients with metal implants.

References

1. Feltes TF, Bacha E, Beekman RH 3rd et al (2011) Indications for cardiac catheterization and intervention in pediatric cardiac disease: a scientific statement from the American Heart Association. Circulation 123:2607–2652
2. Shellock FG, Shellock VJ (1998) Cardiovascular catheters and accessories: ex vivo testing of ferromagnetism, heating, and artifacts associated with MRI. J Magn Reson Imaging 8:1338–1342
3. Spuentrup E, Ruebben A, Mahnken A et al (2005) Artifact-free coronary magnetic resonance angiography and coronary vessel wall imaging in the presence of a new, metallic, coronary magnetic resonance imaging stent. Circulation 111:1019–1026
4. Stevens SM, Tung R, Rashid S et al (2014) Device artifact reduction for magnetic resonance imaging of patients with implantable

cardioverter-defibrillators and ventricular tachycardia: late gadolinium enhancement correlation with electroanatomic mapping. Heart Rhythm 11:289–298

5. Delfaut EM, Beltran J, Johnson G et al (1999) Fat suppression in MR imaging: techniques and pitfalls. Radiogr Rev 19:373–382

6. Spuentrup E, Ruebben A, Stuber M et al (2003) Metallic renal artery MR imaging stent: artifact-free lumen visualization with projection and standard renal MR angiography. Radiology 227:897–902

7. Hargreaves BA, Worters PW, Pauly KB et al (2011) Metal-induced artifacts in MRI. AJR Am J Roentgenol 197:547–555

8. Koch KM, Hargreaves BA, Pauly KB et al (2010) Magnetic resonance imaging near metal implants. J Magn Reson Imaging 32: 773–787

9. Levine GN, Gomes AS, Arai AE et al (2007) Safety of magnetic resonance imaging in patients with cardiovascular devices: an American Heart Association scientific statement from the Committee on Diagnostic and Interventional Cardiac Catheterization, Council on Clinical Cardiology, and the Council on Cardiovascular Radiology and Intervention: endorsed by the American College of Cardiology Foundation, the North American Society for Cardiac Imaging, and the Society for Cardiovascular Magnetic Resonance. Circulation 116:2878–2891

10. Holton A, Walsh E, Anayiotos A et al (2002) Comparative MRI compatibility of 316 L stainless steel alloy and nickel-titanium alloy stents. J Cardiovasc Magn Reson 4:423–430

11. Shellock FG (2001) Prosthetic heart valves and annuloplasty rings: assessment of magnetic field interactions, heating, and artifacts at 1.5 tesla. J Cardiovasc Magn Reson 3:317–324

12. Shellock FG, Valencerina S (2005) Septal repair implants: evaluation of magnetic resonance imaging safety at 3 T. Magn Reson Imaging 23:1021–1025

13. Warnes CA, Williams RG, Bashore TM et al (2008) ACC/AHA 2008 guidelines for the management of adults with congenital heart disease: a report of the American College of Cardiology/American Heart Association Task Force on Practice Guidelines (writing committee to develop guidelines on the management of adults with congenital heart disease). Developed in collaboration with the American Society of Echocardiography, Heart Rhythm Society, International Society for Adult Congenital Heart Disease, Society for Cardiovascular Angiography and Interventions, and Society of Thoracic Surgeons. J Am Coll Cardiol 52:e143–263

14. Silversides CK, Marelli A, Beauchesne L et al (2010) Canadian Cardiovascular Society 2009 consensus conference on the management of adults with congenital heart disease: executive summary. Can J Cardiol 26:143–150

15. Fratz S, Chung T, Greil GF et al (2013) Guidelines and protocols for cardiovascular magnetic resonance in children and adults with congenital heart disease: SCMR expert consensus group on congenital heart disease. J Cardiovasc Magn Reson 15:51

16. Wang Y, Truong TN, Yen C et al (2003) Quantitative evaluation of susceptibility and shielding effects of nitinol, platinum, cobalt-alloy, and stainless steel stents. Magn Reson Med 49:972–976

17. Khan SN, Rapacchi S, Levi DS et al (2013) Pediatric cardiovascular interventional devices: effect on CMR images at 1.5 and 3 tesla. J Cardiovasc Magn Reson 15:54

18. Xue H, Kellman P, Larocca G et al (2013) High spatial and temporal resolution retrospective cine cardiovascular magnetic resonance from shortened free breathing real-time acquisitions. J Cardiovasc Magn Reson 15:102